The Role of Surface Heat Fluxes on the Size of Typhoon Megi (2016)

LI-ZHI SHEN,[a] CHUN-CHIEH WU,[a] AND FALKO JUDT[b]

[a] *Department of Atmospheric Sciences, National Taiwan University, Taipei, Taiwan*
[b] *National Center for Atmospheric Research, Boulder, Colorado*

(Manuscript received 13 May 2020, in final form 7 January 2021)

ABSTRACT: This study attempts to understand how surface heat fluxes in different storm regions affect tropical cyclone (TC) size. The Advanced Research version of the Weather Research and Forecasting (ARW-WRF) Model (version 3.5.1) is used to simulate Typhoon Megi (2016). A series of numerical experiments are carried out, including a control simulation and several sensitivity experiments with surface heat fluxes suppressed in different TC regions [to mimic the reduction of the wind-induced surface heat exchange (WISHE) feedback in the inner and/or outer core]. The results show that with surface heat fluxes suppressed in the entire domain, the TC tends to be smaller. Meanwhile, the TC size is more sensitive to the surface heat flux change in the outer core than to that in the inner core. Suppressing surface heat fluxes can weaken the rainbands around the suppressed area, which in turn slows down the secondary circulation. When the surface heat flux is suppressed in the inner-core region, the weakening of the secondary circulation associated with the diminished inner rainbands is limited to the inner-core region, and only slightly affects the absolute angular momentum import from the outer region, thus having negligible impact on TC size. However, suppression of surface heat fluxes in the outer-core region leads to less active outer rainbands and a more substantial weakening of secondary circulation. This results in less absolute momentum import from the outer region and in turn a smaller TC.

KEYWORDS: Tropical cyclones; Secondary circulation; Surface fluxes

1. Introduction

Intensity and size are the two main characteristics used to describe the damage potential of tropical cyclones (TCs; Marks et al. 1998; Wang and Wu 2004; Cheng and Wu 2018, 2020). The energy source of TCs is surface heat fluxes (Riehl 1950; Zhang and Emanuel 2016), an idea that was cast into a theory called the wind-induced surface heat exchange (WISHE) mechanism (Emanuel 1986, 1989), which highlights the positive feedback between surface heat fluxes and storm intensity. Through the disequilibrium between ocean surface and near-surface atmosphere, TCs extract energy from below (Neelin et al. 1987; Emanuel et al. 1987). The energy enhances the development of convection, leading to more diabatic heat release (Ito et al. 2011). Due to hydrostatic balance, the increased diabatic heating lowers the sea level pressure, strengthening the low level radial and tangential wind. Since the supply of enthalpy flux is related to surface wind speed, the increased surface wind extracts more energy from ocean to TCs. This positive feedback enhances development of TCs.

Surface heat fluxes are the main energy source of TCs, and their magnitude affects TC intensity (Wu et al. 2007; Lin et al. 2009; Xu and Wang 2010a; Lin et al. 2011, 2013; Ma et al. 2013; Wu et al. 2016). Xu and Wang (2010a) reduced surface heat fluxes at different radii and showed that the surface heat fluxes in the eye only slightly affect the intensity, whereas the surface heat fluxes in the eyewall region strongly affect the intensity. Their study showed that surface heat fluxes at 2–2.5 times the radius of maximum wind (RMW) could also affect TC intensity. Moreover, the removal of surface heat fluxes from the outer-core region reduces the RMW, which leads to storm intensification. The authors also suggested that surface heat fluxes in the inner-core region enhance rainband activity, increasing the secondary circulation. Therefore, the increased inflow in the lower level can transport more convective available potential energy into the inner-core region, which is favorable for storm development.

There have been some studies that suggest surface heat fluxes are also important for TC size. For example, Ma et al. (2015) suggested that the removal of sensible heat fluxes leads to a 20% size decrease. Frisius (2015) used an idealized model to investigate the relationship between variables such as planetary rotation and horizontal diffusion in the model and TC size. In one of the experiments, the surface transfer coefficient was changed, and the results showed that a larger surface transfer coefficient leads to a larger TC, which again indicates that the amount of surface heat fluxes can affect TC size. Along similar lines, Radu et al. (2014) changed the atmospheric conditions including the surface heat fluxes and found that the TCs with increased surface heat fluxes are larger than those with reduced surface heat fluxes.

Recently, Cronin and Chavas (2019) used an idealized model to analyze the influence of a dry surface on TCs. They showed that the TCs will weaken when the surface is dry, and their outer radii become smaller as well. Chen and Chavas (2020) used the Cloud Model 1 (CM1) to understand the effect of reduced surface moisture on TC size, and they showed that surface drying results not only in the weakening of TCs, but also the reduction in size. Under a dry condition, the atmosphere is more stable, leading to a weaker secondary circulation. As a consequence, the inward transport of absolute angular momentum (AAM) is reduced and thereby creates the potential for a TC to grow in size. Other studies show that

Corresponding author: Chun-Chieh Wu, cwu@typhoon.as.ntu.edu.tw

DOI: 10.1175/JAS-D-20-0141.1

© 2021 American Meteorological Society. For information regarding reuse of this content and general copyright information, consult the AMS Copyright Policy (www.ametsoc.org/PUBSReuseLicenses).

Unauthenticated | Downloaded 06/06/22 05:55 PM UTC

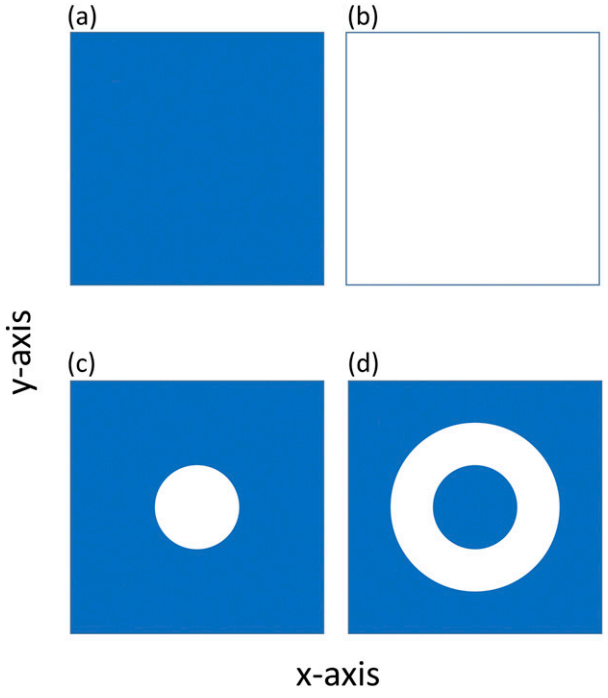

FIG. 1. The schematic diagram of surface heat fluxes in (a) CTL, (b) ALL, (c) R03, and (d) R36. The surface heat fluxes in the blue region are not suppressed. In the white regions, the surface heat fluxes are modified.

AAM import is crucial to TC size as well. Chan and Chan (2012, 2013) used QuikSCAT data to analyze TC features, and indicated that the outflow in the upper levels is stronger in intense TCs, while it is weaker in less intense TCs. As for TC size, which Chan and Chan (2013) defined as the radius of the wind speed of 17 m s^{-1} at 10-m height (hereafter R17), larger TCs have comparatively higher AAM import in the lower level, while the AAM import in smaller TCs is constrained to a very limited area. The above results emphasize the importance of low-level AAM import. Chan and Chan (2014) used an idealized model to investigate the effect of initial vortex size. Their results showed that a larger initial vortex could grow into a larger TC because it transports more angular momentum into the vortex. On the contrary, a small initial vortex remains small. A small TC can grow nonetheless into a large TC when it has a long lifetime because it has more time to transport angular momentum into the vortex.

Hill and Lackmann (2009) suggested that moist environments favor TC size (R17) increase. In a moist environment, the outer rainbands are more active, generating more potential vorticity. The vorticity would be transported into TCs and would facilitate size increase. The studies from Hill and Lackmann (2009) and Chan and Chan (2013, 2014) indicated that the low-level inflow of TCs plays a role in TC size changes. Besides the environmental conditions, TCs in different basins have different size growth rates. In general, TCs in the western North Pacific (WNP) are larger than those in the North Atlantic (NA), and are associated with greater growth rate and

TABLE 1. The name, the extent of suppressed area, and the amount of surface heat fluxes of all the experiments. The surface heat fluxes are reduced by 40%, 50%, 60%, and 70% (ε = 0.4, 0.5, 0.6, and 0.7, respectively) from the original value in the entire innermost domain (ALL), in the inner-core region (R03, 0–180 km), and in the outer-core region (R36, 180–360 km).

Expt	Suppressed region	ε
CTL	No	1
ALLF70	Innermost domain	0.7
ALLF60	Innermost domain	0.6
ALLF50	Innermost domain	0.5
ALLF40	Innermost domain	0.4
R03F70	0–180 km	0.7
R03F60	0–180 km	0.6
R03F50	0–180 km	0.5
R03F40	0–180 km	0.4
R36F70	180–360 km	0.7
R36F60	180–360 km	0.6
R36F50	180–360 km	0.5
R36F40	180–360 km	0.4

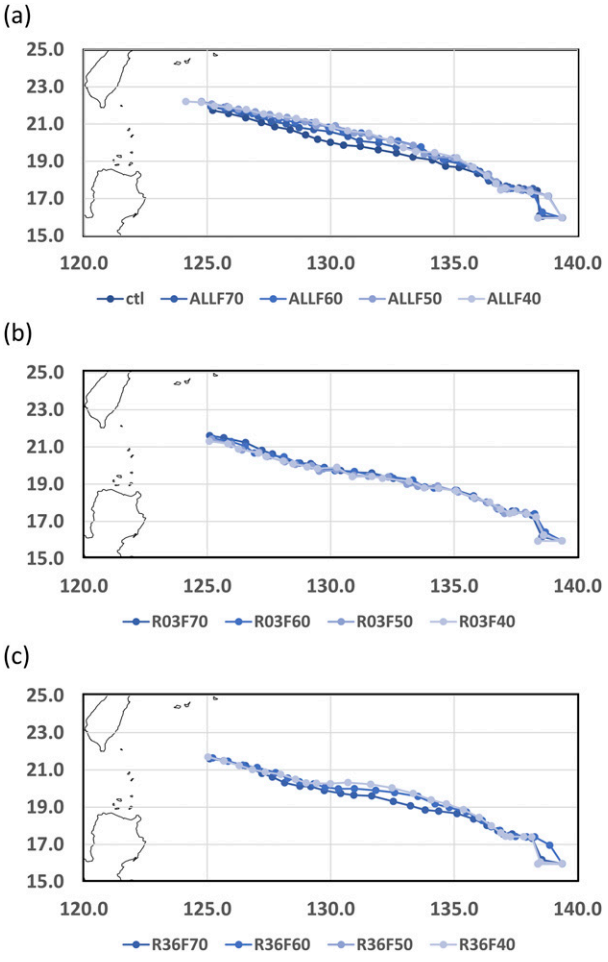

FIG. 2. The tracks of (a) ALL, (b) R03, and (c) R36 from 1 to 79 h. The time interval is 3 h.

Unauthenticated | Downloaded 06/06/22 05:55 PM UTC

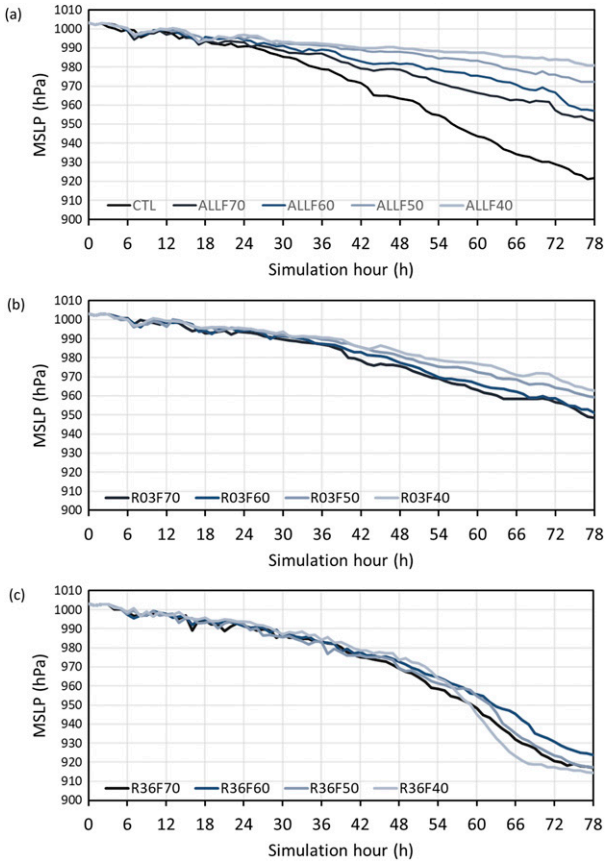

FIG. 3. The evolution of minimum sea level pressure of (a) ALL, (b) R03, and (c) R36.

earlier lifetime peak in TC size (Liu and Chan 2002; Chavas and Emanuel 2010; Lee et al. 2010; Lu et al. 2011; D'Asaro et al. 2013; Knaff et al. 2014; Chan and Chan 2015; Schenkel 2017).

Tsuji et al. (2016) used an idealized model to simulate the relationship between rainbands and TC size, defined as the radius of the wind speed of 15 m s^{-1} at 10-m height. In their study, the thermal forcing, which can be regarded as a manifestation of rainbands, is located at different radii in each simulation. They divided those experiments into three scenarios. In the first scenario, the location of forcing is close to the TC center. Because of the large inertial stability near TC center, the forcing-induced secondary circulation is narrow and constrained in the inner-core region, and unable to transport AAM around the lateral boundary of TCs. Since the AAM in the lower level could not be transported into the lateral boundary of TCs, the size of TCs is small. In the second scenario, the location of forcing is further away from the TC center than that in the first scenario, but is still in the inner side of TC lateral boundary. In this case, the AAM could be transported into TCs with smaller inertial stability, which is favorable for size increase. In the last scenario, the forcing is located outside of the TC lateral boundary, and thus the induced secondary circulation transports AAM outward, which is unfavorable for the size increase. In conclusion, the location

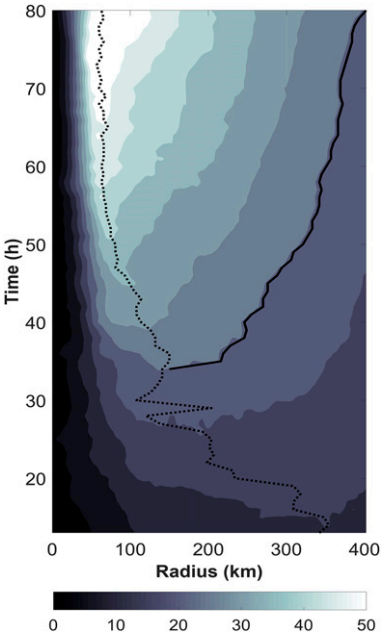

FIG. 4. The Hovmöller diagram of azimuthally averaged wind speed (shaded, m s^{-1}) at 2-km height of CTL. The RMW (dashed line) and size (solid line) are also defined at 2-km height.

of rainbands is crucial for low-level AAM import, which affects changes in TC size.

Previous studies have implied that surface heat fluxes play a role in determining TC size. As mentioned in Tsuji et al. (2016), the location of rainbands is crucial for size growth, and since the surface heat fluxes in different locations affect the rainbands in different regions, the surface heat fluxes in different locations may have different impacts on TC size. Therefore, it is worth understanding the impact of surface heat fluxes around the eyewall region, since the fluxes are known to be an important source of intensification, particularly those in the outer region, which are critical for determining the rainbands. In this study, we attempt to address the following two issues: 1) How do surface heat fluxes at different storm locations affect TC size (Shen and Wu 2018), and 2) since the WISHE mechanism serves as the linkage that explains impact of surface heat fluxes on TC intensity, can surface heat fluxes be related to TC size as well through the WISHE mechanism?

The description of the model and of the experiments is in section 2. Section 3 presents an analysis of the structural changes, including diabatic heating, secondary circulation, low-level inflow and AAM transport differences. The summary and conclusions are given in section 4.

2. Model and experiment designs

a. Typhoon Megi (2016)

The subject of this study is Typhoon Megi (2016). Megi was an uncharacteristically large TC and therefore an ideal case for the purpose of this study (i.e., the reduction of surface heat fluxes in the inner and/or outer regions in a large TC is more

Unauthenticated | Downloaded 06/06/22 05:55 PM UTC

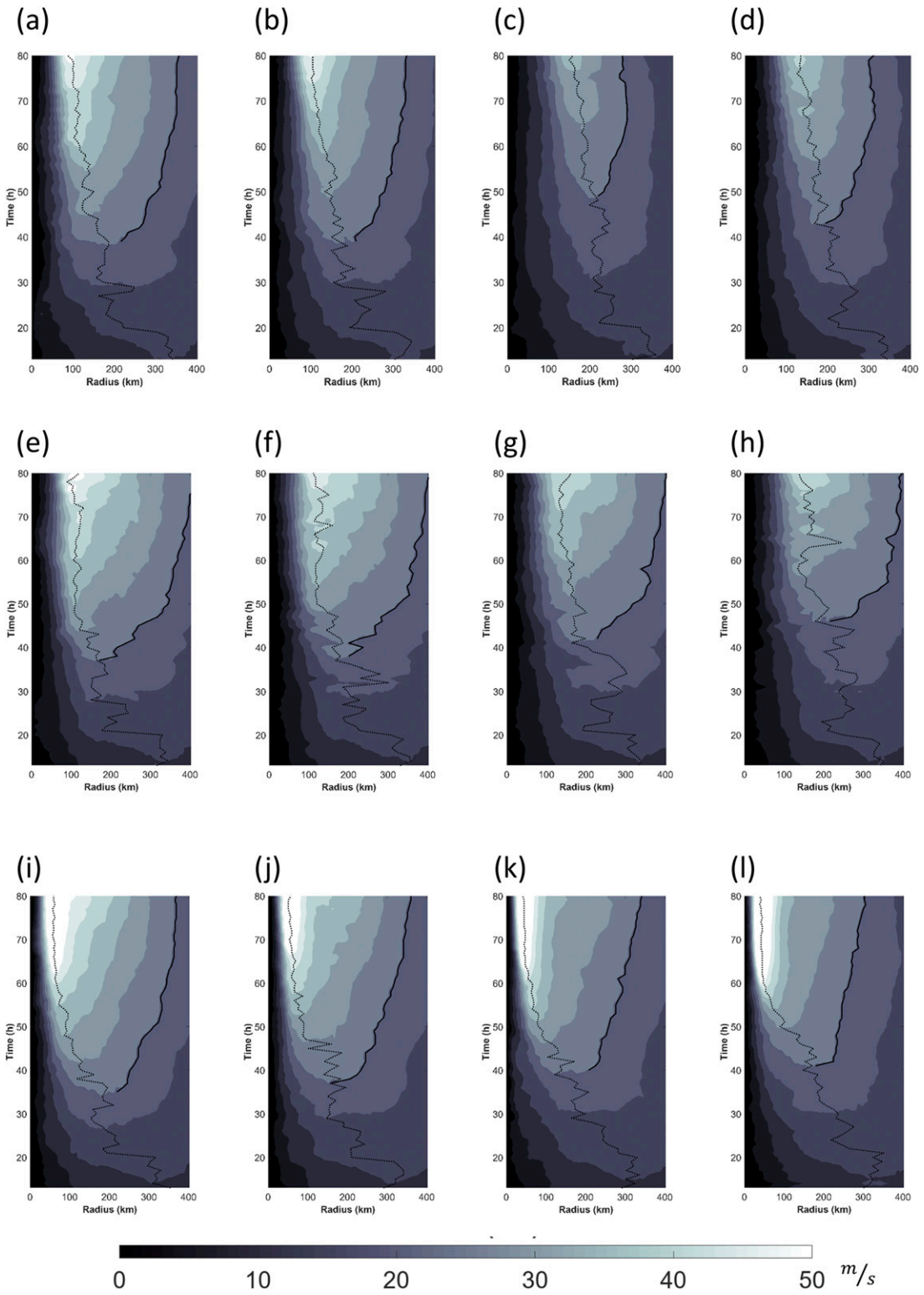

FIG. 5. As in Fig. 4, but for (a) ALLF70, (b) ALLF60, (c) ALLF50, (d) ALLF40, (e) R03F70, (f) R03F60, (g) R03F50, (h) R03F40, (i) R36F70, (j) R36F60, (k) R36F50, and (l) R36F40.

Unauthenticated | Downloaded 06/06/22 05:55 PM UTC

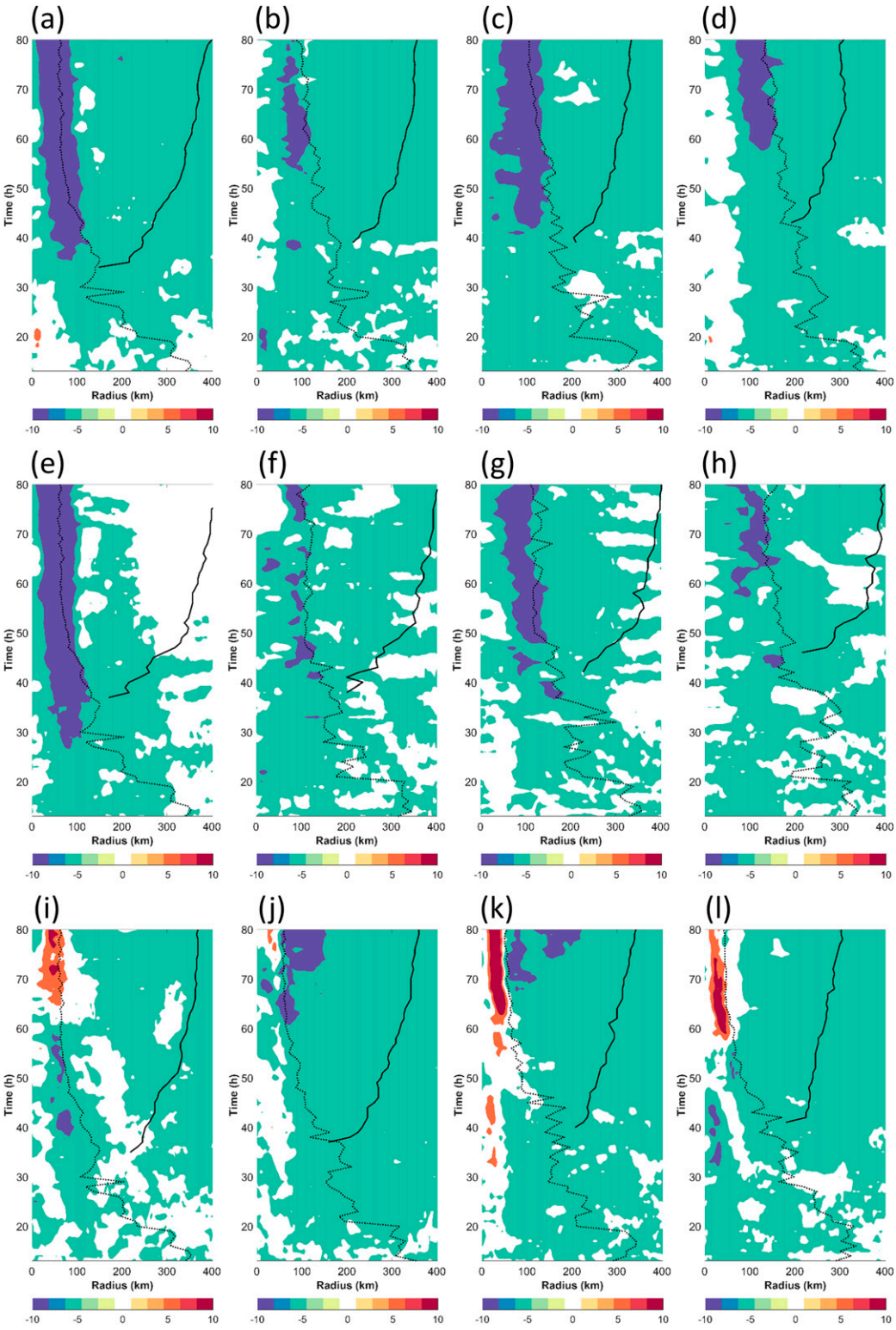

FIG. 6. The Hovmöller diagram of the difference of azimuthally averaged wind speed (shaded, m s^{-1}) at 2-km height between (a) ALLF70 and CTL, (b) ALLF60 and ALLF70, (c) ALLF50 and ALLF60, (d) ALLF40 and ALLF50, (e) R03F70 and CTL, (f) R03F60 and R03F70, (g) R03F50 and R03F60, (h) R03F40 and R03F50, (i) R36F70 and CTL, (j) R36F60 and R36F70, (k) R36F50 and R36F60, and (l) R36F40 and R36F50. The RMW (dashed line) and size (solid line) of (a) ALLF70, (b) ALLF60, (c) ALLF50, (d) ALLF40, (e) R03F70, (f) R03F60, (g) R03F50, (h) R03F40, (i) R36F70, (j) R36F60, (k) R36F50, and (l) R36F40 are also defined at 2-km height.

Unauthenticated | Downloaded 06/06/22 05:55 PM UTC

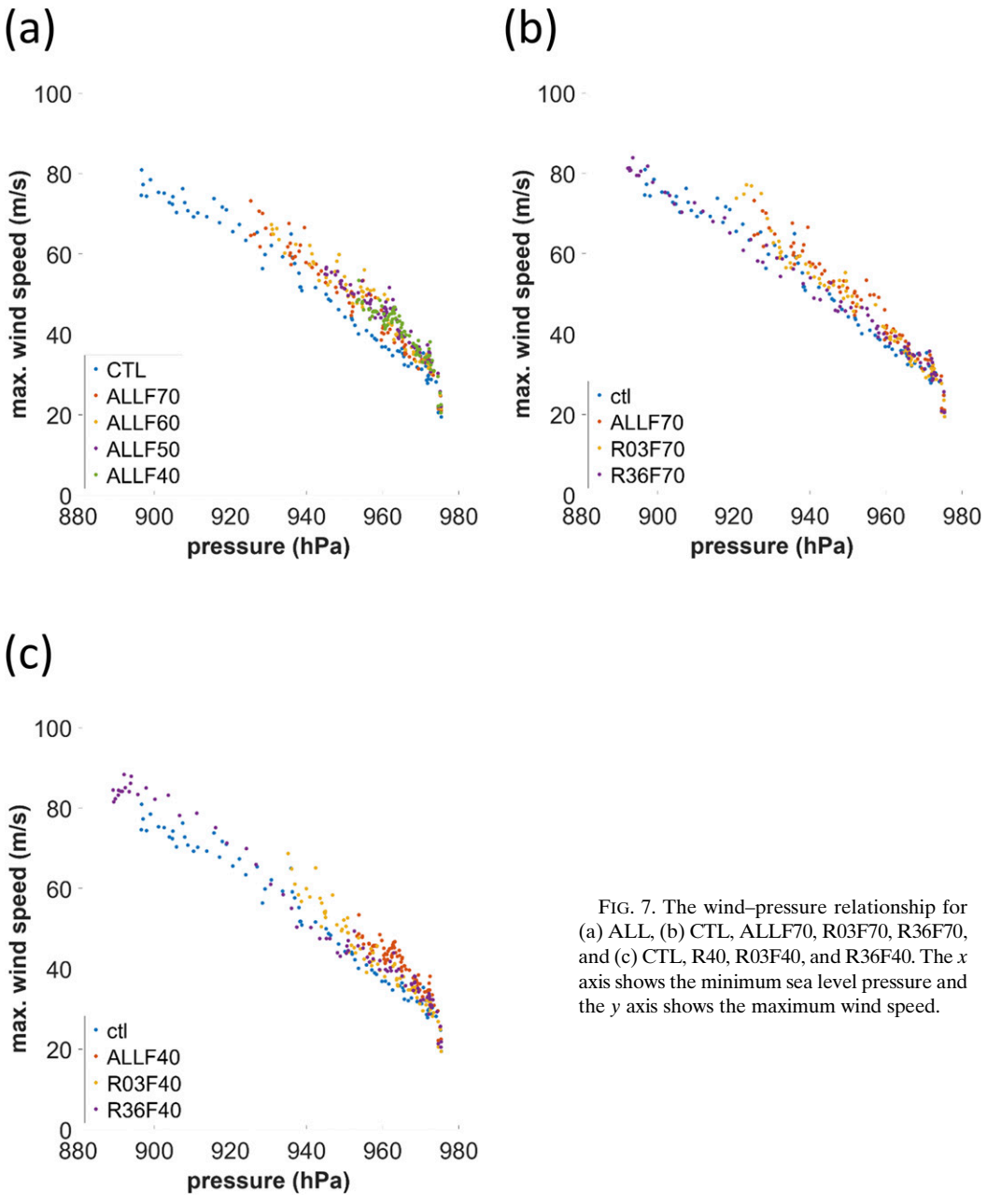

FIG. 7. The wind–pressure relationship for (a) ALL, (b) CTL, ALLF70, R03F70, R36F70, and (c) CTL, R40, R03F40, and R36F40. The x axis shows the minimum sea level pressure and the y axis shows the maximum wind speed.

distinct than that in a small TC). According to the best track data from the Joint Typhoon Warning Center (JTWC), Megi formed at 0012 UTC 23 September 2016 in the western North Pacific, after which it began moving northwestward. The size (R17) of Megi grew to 240 km with the intensity reaching 952 hPa at 0000 UTC 26 September before the typhoon approached the Philippines.

b. *Numerical simulations*

The numerical simulations [i.e., the control run (CTL) and sensitivity experiments] of this study are performed with the Advanced Research Version of the Weather Research and Forecasting (WRF-ARW) Model (version 3.5.1). The initial conditions are derived from the final analysis data of National Centers for Environmental Prediction (NCEP). All of the simulations have three nested domains with grid spacings of 27, 9 and 3 km, i.e., 181 × 130, 223 × 223, and 334 × 334 grid points, respectively. The model is set up with 34 eta (η) levels in the vertical, with relatively higher vertical resolution in the boundary and outflow layers, and the model top is set at 50 hPa. The microphysics scheme WSM6 and the Yonsei University planetary boundary layer scheme (Hong et al. 2006) are used in every domain, whereas the Kain–Fritch cumulus scheme (Kain and Fritsch 1990; Kain 2004) is only used in the two outer

Unauthenticated | Downloaded 06/06/22 05:55 PM UTC

domains. Longwave radiation and short wave radiation are parameterized with the Rapid Radiative Transfer Model (RRTM) scheme (Iacono et al. 2000) and the simple short wave Dudhia scheme (Ruiz-Arias et al. 2013), respectively, while the MM5 similarity scheme (Paulson 1970; Dyer and Hicks 1970; Webb 1970; Zhang and Anthes 1982; Beljaars 1995; Jiménez et al. 2012) is applied to parameterize processes in the surface layer.

The simulations are initialized at 0000 UTC 23 September 2016, when Megi is still a tropical disturbance, and integrated for five days (120 h). The subsequent analysis focuses, however, on the time before 80 h to exclude the period in which the TC is affected by the presence of Taiwan's terrain.

c. *Sensitivity experiments*

As the focus of this study is on the role of surface heat fluxes, it may be worthwhile to review the equations for sensible heat flux (SH) and latent heat flux (LH). The equations are as follows:

$$\mathrm{LH} = \varepsilon \rho L_v C_q U_{10}(q_s - q_a), \tag{1}$$

$$\mathrm{SH} = \varepsilon \rho C_p C_h U_{10}(\theta_s - \theta_a), \tag{2}$$

where ρ is the air density; C_q and C_h are the exchange coefficients for the enthalpy and momentum transfer, respectively; L_v is the latent heat of vaporization; c_p is the specific heat capacity of air at constant pressure; U_{10} is the 10-m wind speed; q_a and θ_a represent the specific humidity and potential temperature at a specific height, respectively; q_s (θ_s) is the specific humidity (potential temperature) of sea surface; and ε is a multiplier for modifying the effect of the WISHE mechanism. When the value of ε is smaller than 1, the surface heat fluxes are less than those in CTL, indicating that the surface heat fluxes are suppressed.

Three groups of experiments are conducted. The first group (Fig. 1b) consists of experiments in which surface heat fluxes are reduced in the entire innermost domain, hereafter ALL (Table 1). The second group (Fig. 1c) and the third group (Fig. 1d) each consists of experiments in which surface heat fluxes are suppressed in the inner-core and outer-core region, respectively. From here on, the second and third groups are referred to as R03 and R36, respectively.

To define the inner-core and outer-core regions, we use the azimuthally averaged RMW of CTL at 2-km height after 60 h (R_m; this value is equivalent to 60 km). Specifically, the inner-core region is defined as 0 to 3 times R_m, ranging from 0 to 180 km, and the outer-core region is defined as 3 to 6 times R_m, ranging from 180 to 360 km. R03 is designed to investigate the surface heat fluxes associated with the eyewall in the inner-core region, while R36 is set up to understand the role of the surface heat fluxes outside the inner core within 3 to 6 times R_m. Note that although the exact region of inner and outer cores changes as the RMW changes, the inner-core region in our simulation contains the RMW, indicating that the surface heat fluxes under the eyewall region are always suppressed in R03 despite the change of RMW. Similarly, the outer-core region in our simulation can generally cover the outer region of TCs, implying that the surface heat fluxes, which influence the rainbands in the outer region, are always reduced in R36. Each group

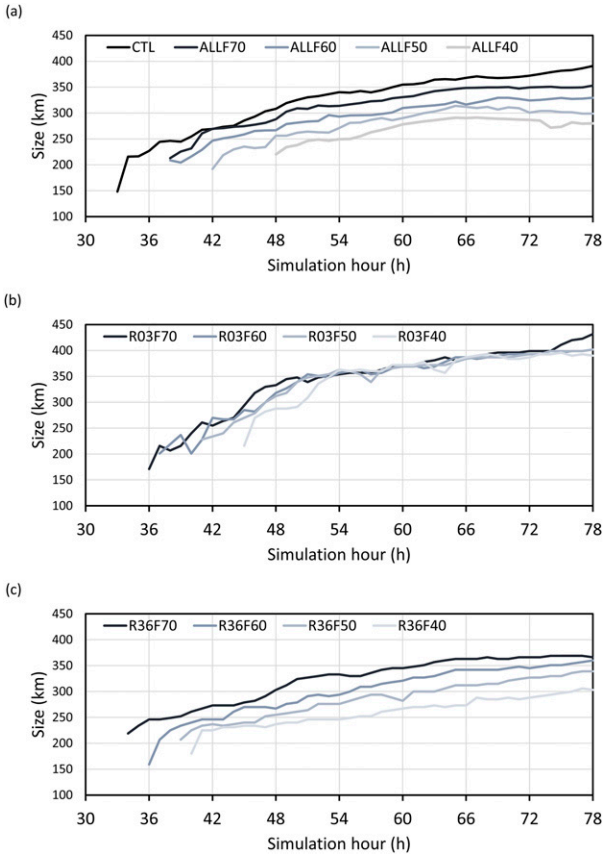

FIG. 8. As in Fig. 3, but for size evolution. The size is defined as the radius where the wind speed at 2-km height is 25 m s^{-1}.

consists of four individual simulations that differ in the amount of surface heat flux reduction. More concretely, the surface heat fluxes are reduced to 40%, 50%, 60%, and 70% of the original value in all of the inner (R03), outer (R36), and entire (ALL) regions. The surface heat fluxes are suppressed from the initial time onward.

The TC size in this study is defined as the radius averaged in all azimuthal directions with 25 m s^{-1} wind at 2-km height. Note that the definition used here is different from the conventional definition of the radius of gale-force surface wind. There are two reasons why we choose the 2-km height to define TC size. First, we want to highlight the TC structure change in the free atmosphere rather than in the boundary layer. Second, since we only suppress the surface heat fluxes in a specific region (inner and outer core), the surface wind is discontinuous around the radius of 3 times R_m (180 km away from TC center), leading to a second peak of surface wind. This discontinuity appears to range from the surface to around 1.5-km height. To avoid this discontinuity from affecting our analyses, the TC size is defined at 2-km height. According to Powell et al. (2003), for typical tropical cyclones the ratio of the wind speed at 2-km and 10-m heights is nearly constant. Therefore, we first calculate the ratio of wind speed at those two heights in CTL, and found that the wind speed of 17 m s^{-1} at 10 m-height corresponds to 25 m s^{-1} at 2-km height at the same position. In CTL, defining the TC size

Unauthenticated | Downloaded 06/06/22 05:55 PM UTC

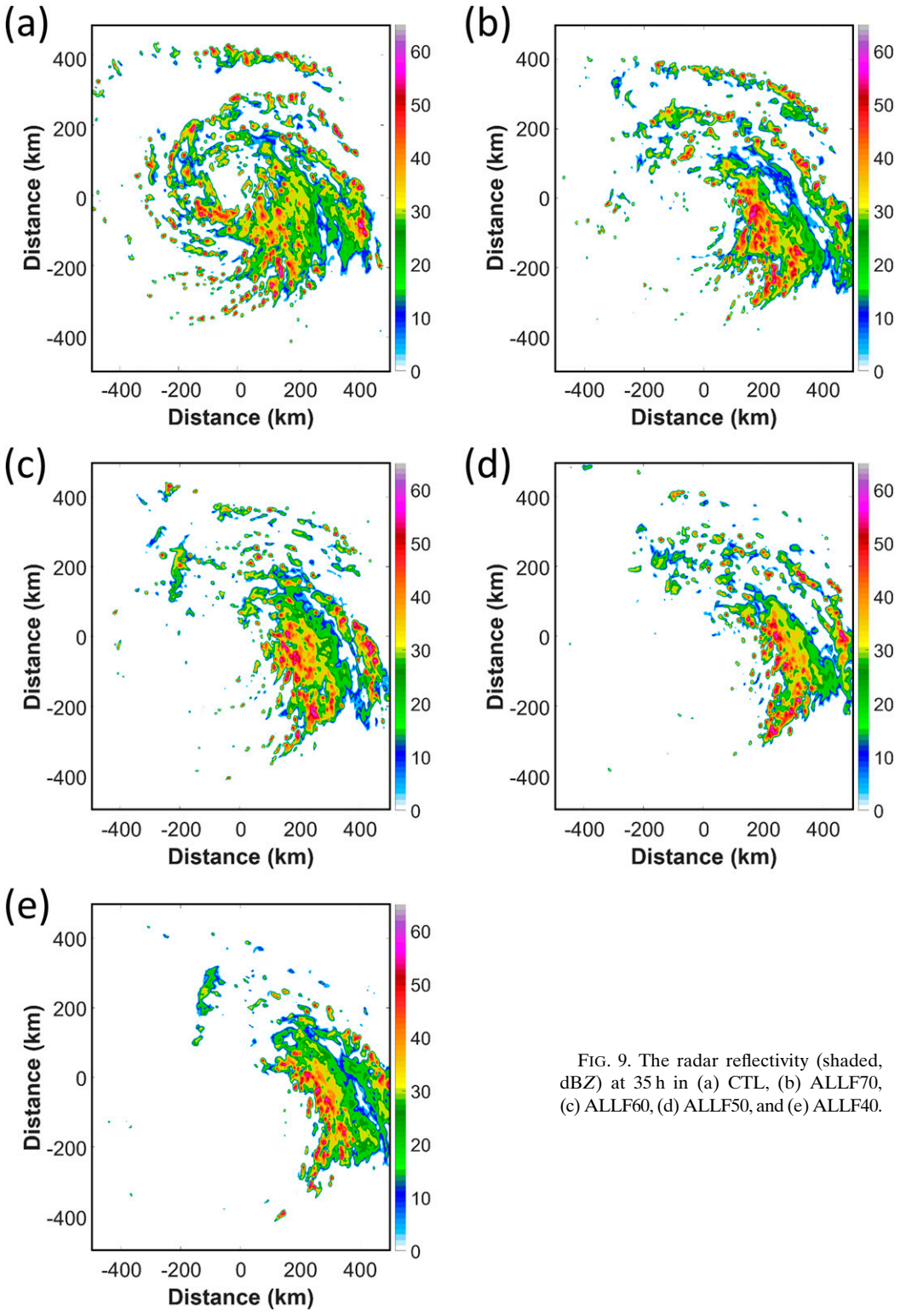

FIG. 9. The radar reflectivity (shaded, dBZ) at 35 h in (a) CTL, (b) ALLF70, (c) ALLF60, (d) ALLF50, and (e) ALLF40.

Unauthenticated | Downloaded 06/06/22 05:55 PM UTC

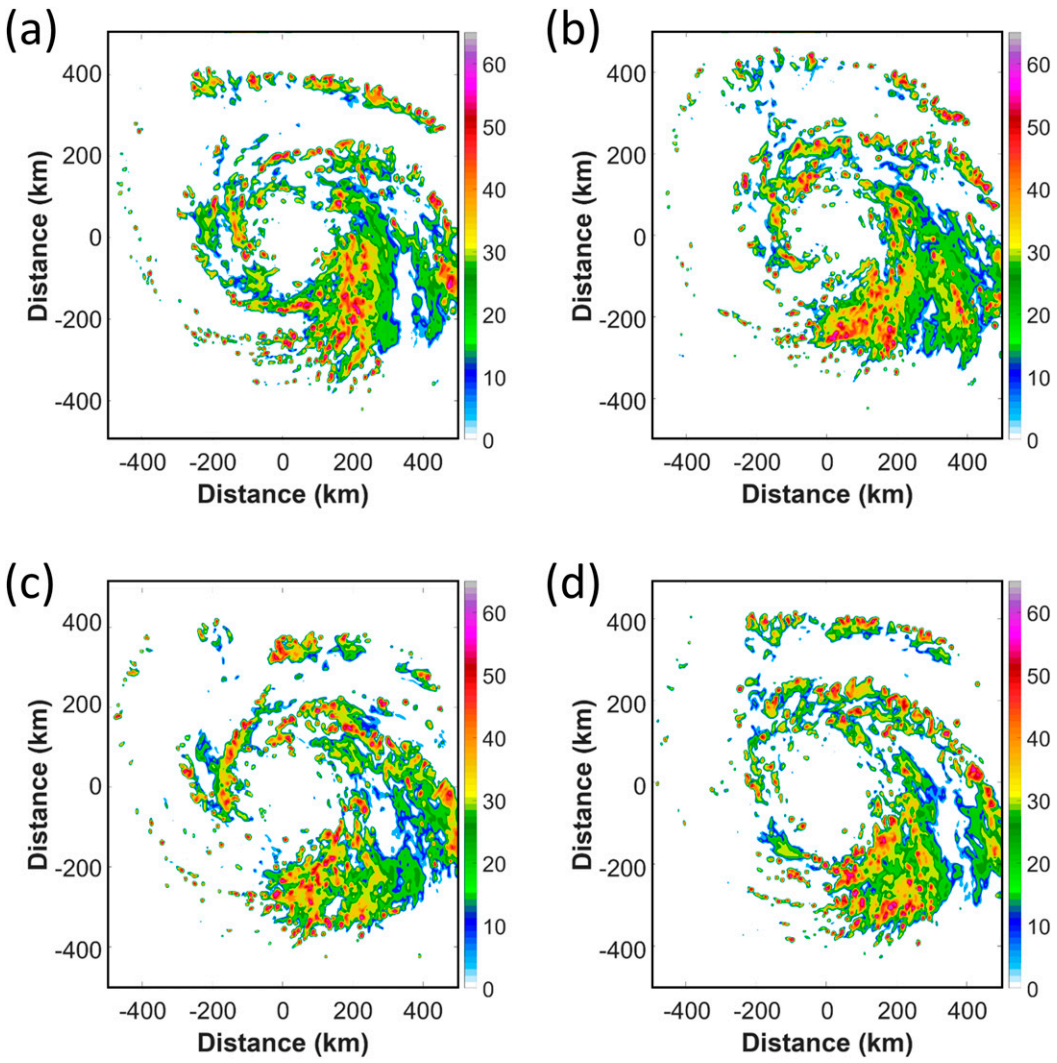

FIG. 10. As in Fig. 9, but for (a) R03F70, (b) R03F60, (c) R03F50, and (d) R03F40.

with traditional criteria or with our criteria would basically lead to the same results. Therefore, the TC size is defined as the radius with 25 m s^{-1} wind at 2-km height in our experiments.

3. Results

a. The evolution of intensity and size

Figure 2 shows the tracks of all the simulations. Generally speaking, the reduction of surface heat fluxes does not affect the tracks, except for some slight variations of less than 1°. Given the limited variability in track, the sea surface temperatures are very similar. In the ALL experiments, less surface heat fluxes leads to weaker TCs (Fig. 3a). The minimum sea level pressure (MSLP) of CTL is 920 hPa at 80 h; this is the strongest within ALL. In general, TCs in the experiments with reduced surface heat fluxes are always weaker than those with comparatively larger surface heat fluxes. For R03 (Fig. 3b), the influence of surface heat fluxes on TC intensity is similar to ALL. In comparison to R03F40, ALLF40 is weaker. This is not surprising since ALLF40 has less surface heat fluxes. However, ALLF70 is more intense than R03F70 despite comparatively less heat fluxes. This indicates that although surface heat fluxes can affect TC intensity, they are not the only dominating factor, and that the location of surface heat fluxes as mentioned in Xu and Wang (2010a) is also important (Peng and Wu 2020). The evolution of intensity in R36 is more complicated. The amount of surface heat fluxes in all R36 experiments is less than those in CTL (Fig. 3c), but the MSLP of R36F50, R36F60, and R36F70 reach 920 hPa at 80 h, meaning the respective TCs are as strong as the one in CTL. R36F40 has the least surface heat fluxes among the R36 experiments, but it becomes stronger than the other experiments at 80 h. This is consistent with the previous study which indicated that the removal of surface heat fluxes in the outer-core region may lead to a stronger TC (Xu and Wang 2010a).

In terms of wind, the intensity of CTL reaches its maximum at 78 h (Fig. 4) with a maximum azimuthally averaged wind speed of 60 m s^{-1} at the RMW of 60 km. The wind field

Unauthenticated | Downloaded 06/06/22 05:55 PM UTC

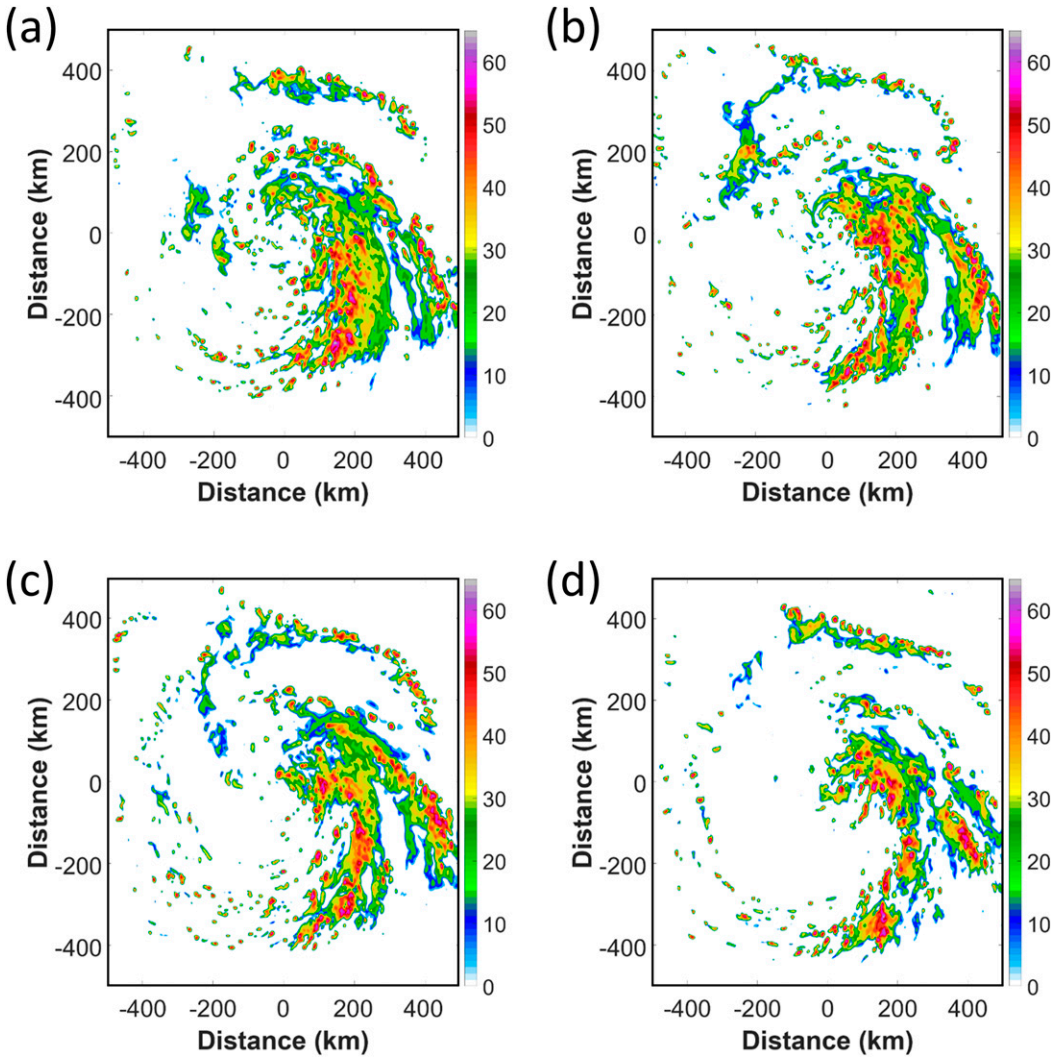

FIG. 11. As in Fig. 9, but for (a) R36F70, (b) R36F60, (c) R36F50, and (d) R36F40.

gradually expands throughout the simulation, and the TC size reaches over 300 km after 50 h, with a lifetime maximum size of 380 km. In ALL, both the wind speed and size decrease with the reduction of surface heat fluxes (Figs. 5a–d), while the RMW decreases over time. Although the wind speed decreases with the suppression of surface heat fluxes in R03, the size does not systematically change with the modification of surface heat fluxes (Figs. 5e–h). Figure 6 emphasizes the trend in the response to the reduction of surface heat fluxes. In Fig. 6a, the azimuthally averaged wind speed in ALLF70 is weaker than that in CTL during the entire simulation period in both inner and outer cores. In ALL (Figs. 6a–d), less surface heat fluxes lead to smaller TCs. In Fig. 6e, the azimuthally averaged wind speed in R03F70 is weaker than that in CTL during the simulation only in the inner-core region. Different from ALL, although the wind speed in the inner-core region in R03 decreases with reduced surface heat fluxes, the change of the wind speed in the outer-core region is relatively small (Figs. 6e–h). In Fig. 6i, the azimuthally averaged wind speed in R36F70 is weaker than that in CTL despite that the difference is not distinct in the region 150–250 km away from the TC center. Same as in ALL, the wind speed systematically decreases with the reduction of outer-core-region surface heat fluxes.

Figure 6 also highlights that the wind speed in the experiments of more surface heat fluxes is stronger than that in the experiments with less surface heat fluxes during the simulation in spite of the eyewall region after 50 h in R36. In ALL, the size decreases with the cut back of surface heat fluxes, accompanied by the weakening of the wind speed. In R03, the size does not systematically change because the wind speed does not dramatically differ among R03. In R36, since the surface heat fluxes are reduced in the outer-core region, the wind speed in that region is decreased, leading to smaller TCs. Note that due to differences in the amount and location of surface heat fluxes, the wind–pressure relationship changes with the modification (Fig. 7). The slope of the relationship in ALL is steeper with the reduction of surface heat fluxes (Fig. 7a). The wind–pressure relationship in R36 is closer to CTL than R03

Unauthenticated | Downloaded 06/06/22 05:55 PM UTC

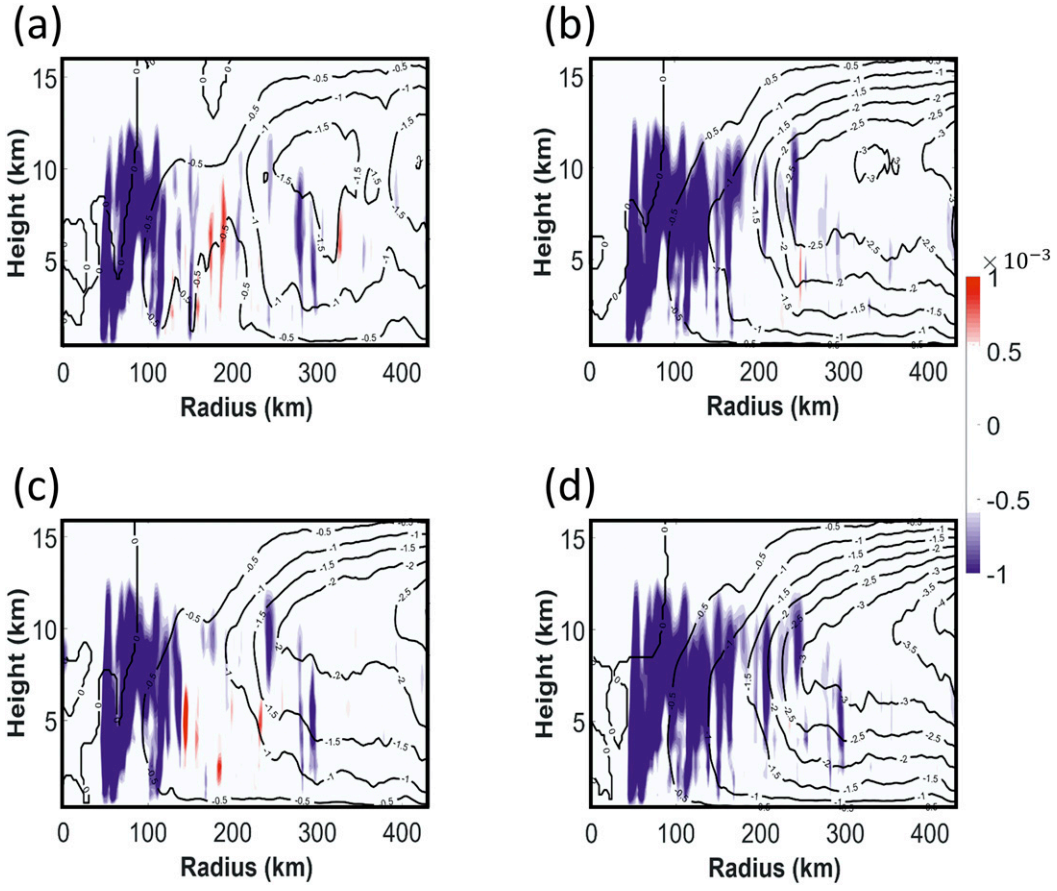

FIG. 12. The difference of azimuthally averaged diabatic heating and streamfunction between CTL and each of (a) ALLF70, (b) ALLF60, (c) ALLF50, and (d) ALLF40 at 35 h. Shading and contours are the diabatic heating ($K\,s^{-1}$) and streamfunction ($10^9\,kg\,s^{-1}$) difference between the simulations and CTL, respectively. The negative value of streamfunction indicates that the reduced secondary circulation is weaker than that in CTL, and the positive value indicates that the secondary circulation is stronger than that in CTL.

(Fig. 7a). The reason of the change due to the reduction of surface heat fluxes and whether this change is significant still require further investigation.

Figure 8 shows the size evolution of all the sensitivity experiments. For the ALL and R36 experiments, reduced surface heat fluxes lead to smaller TCs (Figs. 8a,c). At 70 h, the size of ALLF40 is only 220 km, in comparison to 380 km of CTL. The sizes of R36F40, R36F50, R36F60, and R36F70 are 300, 340, 350, and 370 km, respectively. However, for the R03 experiment, the size differences among the simulations are not distinct. The sizes of all R03 experiments are around 350 km, indicating that surface heat fluxes have only limited impact on TC sizes although their amount in R03 experiments are different. Therefore, the location of surface heat fluxes seems crucial to TC size. The outer-core surface heat fluxes seem to be more important than those in the inner-core region, and more surface heat fluxes in the outer-core region lead to larger TCs.

b. The rainband and precipitation

Figures 9–11 are plan views of radar reflectivity at 35 h. The period of 35 h is chosen to represent the early stage of the simulations. Here, we attempt to understand the variability in TC structure that is associated with the reduction of surface heat fluxes, so we focus on the time period in which the structure of those simulations becomes different. The radar reflectivity is stronger and more symmetric in CTL (Fig. 9) than in the other simulations. Once surface heat fluxes are reduced, the reflectivity signature weakens, indicating that the reduction of enthalpy flux reduces rainband activity. In R03, although the surface heat fluxes are different, the distribution and magnitude of radar reflectivity in the outer-core region differ only slightly among the four runs (Fig. 10). The storms in R36 are more asymmetric than those in the R03 experiment (Fig. 11). The rainbands are mostly located on the southeast side, and are weakest in R36F40. Overall, the inner-core surface heat fluxes only slightly affect the distribution and the strength of the rainbands, whereas the outer-core surface heat fluxes dominate the rainband activity in the outer-core region.

Figures 12–14 show the diabatic heating and streamfunction differences between each simulation and CTL. In ALL, the overall diabatic heating is weaker than CTL (Fig. 12). In the R03 experiment, the reduction of diabatic heating is located in

Unauthenticated | Downloaded 06/06/22 05:55 PM UTC

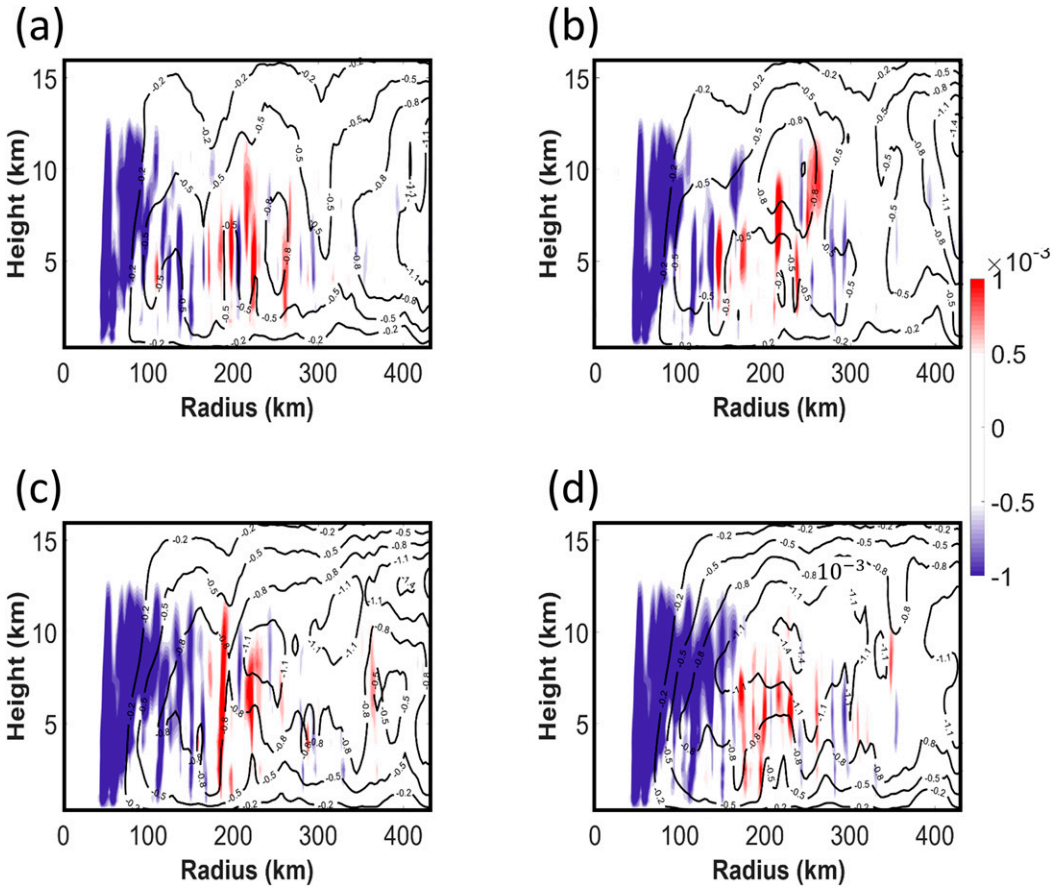

FIG. 13. As in Fig. 12, but for (a) R03F70, (b) R03F60, (c) R03F50, and (d) R03F40.

the inner-core region, especially in the innermost 150 km (Fig. 13). As for ALL, less surface heat fluxes result in reduction of diabatic heating in R03. The diabatic heating in the inner-core region in R03F40 is the weakest among R03 experiments. In the R36 experiments, the diabatic heating in the outer-core region is weaker than that in CTL, and similar to the other sensitivity experiments, the reduction of surface heat fluxes leads to less diabatic heating in the outer-core region (Fig. 14). At 60 h, the patterns between the simulations are the same but with larger values, indicating that the evolution of the experiments is completely distinct among ALL, R03 and R36, and the differences grow with time (figures not shown). Note that there is strong diabatic heating increase within 50 km. According to Xu and Wang (2010b), less surface heat fluxes lead to a smaller RMW. In our study, since the surface heat fluxes are reduced in R36, the RMW in the sensitivity experiments is smaller than that in CTL.

c. Circulation

Due to the different diabatic heating and inertial stability distribution, the induced secondary circulation in the sensitivity experiments is different from CTL. Studies show that the overturning circulation tends to be elongated vertically in the region with large inertial stability, while in the area with smaller inertial stability, the overturning circulation is elongated more horizontally (Holland and Merrill 1984; Willoughby 1995). The inertial stability in the inner core is larger than that in the outer-core region, so if the diabatic-induced secondary circulation is located in the inner core, the circulation will be radially narrow. In contrast, if the induced secondary circulation is located in the outer-core region, the circulation will be broader because of the smaller inertial stability. In this study, the streamfunction (Ψ) is used to represent the secondary circulation. It is calculated as follows:

$$\Psi = \int_0^z -r\rho v_r \, dz \,, \tag{3}$$

where r is the radial distance from TC center, ρ is the air density, and v_r is the radial wind. A negative streamfunction difference indicates that the radial circulation in a given sensitivity simulation is weaker than that in CTL. In ALL (Fig. 12), reducing surface heat fluxes in the entire domain leads to the weakening of the secondary circulation. The weaker diabatic heating in the inner-core region is associated with the weaker upward motion, accompanied by a weaker secondary circulation. The rainbands in the inner and outer core are weaker because of the reduction of surface heat fluxes at all radii. Therefore, the secondary circulation is weaker both in the inner and outer core. In R03 (Fig. 13), similar to ALL, the reduction in surface heat fluxes leads to a weaker secondary

Unauthenticated | Downloaded 06/06/22 05:55 PM UTC

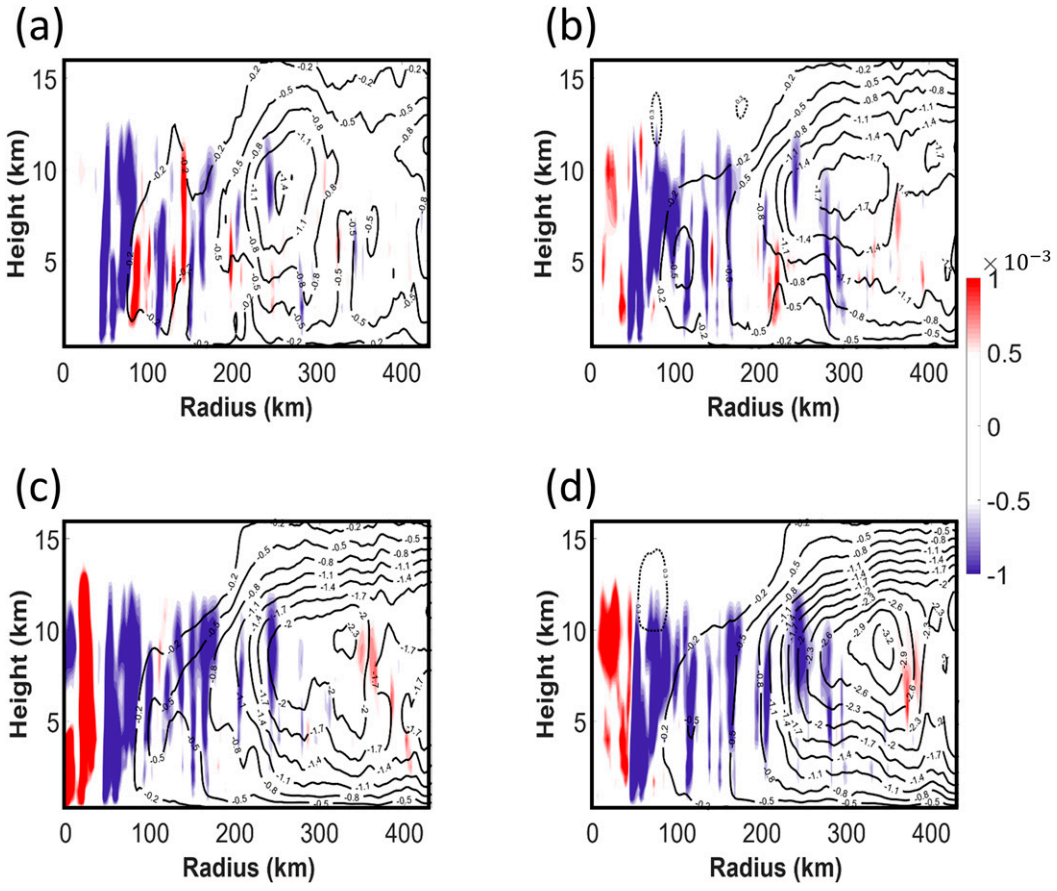

FIG. 14. As in Fig. 12, but for (a) R36F70, (b) R36F60, (c) R36F50, and (d) R36F40.

circulation. However, due to the increase of diabatic heating around 200 km away from TC center, the upward motion around 200 to 300 km from TC center is stronger than that in CTL. In the outer region of the TCs (300 to 400 km away from TC center), the gradient of the streamfunction remains consistent among R03 experiments, indicating that the systematic reduction of surface heat fluxes in the inner-core region only slightly affects the low-level inflow in the outer region. In R36 (Fig. 14), the suppression of surface heat fluxes leads to the weakening of overturning circulation. Moreover, the amount of surface heat fluxes reduction strongly weakens the secondary circulation in the outer-core region. When the weakening of the secondary circulation is compared between R36F70 and R36F40 (Figs. 14a,d), the gradient of the streamfunction in the low level around 300 to 400 km away from the TC center in R36F40 is much stronger than that in R03F70, suggesting that the low-level inflow in this region is different. In brief, the decrease of diabatic heating results in the weakening of the secondary circulation. The secondary circulation difference only slightly changes among R03 in the outer-core region while the secondary circulation in the outer core weakens with the suppression of surface heat fluxes among R36. The weakening in the outer region is more distinctly changed in R36 than in R03, leading to weaker low-level inflow in the outer region in R36.

The strength of the secondary circulation affects the strength of the low-level inflow. Figure 15 shows the inflow in the ALL simulations below 2 km. Since the secondary circulation becomes weaker as the surface heat fluxes decrease, the low-level inflow is strongest in CTL and weakest in ALLF40. The area of inflow ranges from around 70-km radius to the outermost region. In R03 (Fig. 16), the inflow is strongest in R03F70 due to the high surface heat fluxes, and weakest in R03F40 due to its low surface heat fluxes. Compared to ALL, the low-level inflow region in R03 is located radially farther out. In R36 (Fig. 17), reducing the surface heat fluxes leads to weaker and shallower low-level inflow. The inflow is stronger than that in the R03 experiments in the inner-core region, but it is weaker in the outer region. Figure 18 demonstrates the difference of low-level inflow between the sensitivity experiments and CTL. It is obvious that the region of the low-level inflow deceleration is located in the inner region of TCs within 100 to 200 km, while the low-level inflow in the outer region only slightly decreases in R03 (Figs. 18a,b). In R36, the low-level inflow decelerates in both the inner and outer regions of TCs, indicating that the response of low-level inflow to the reduction of surface heat fluxes in inner and outer cores are different. The strength of the low-level inflow strongly affects low-level AAM transport, so the AAM transport is different between R03 and R36.

Unauthenticated | Downloaded 06/06/22 05:55 PM UTC

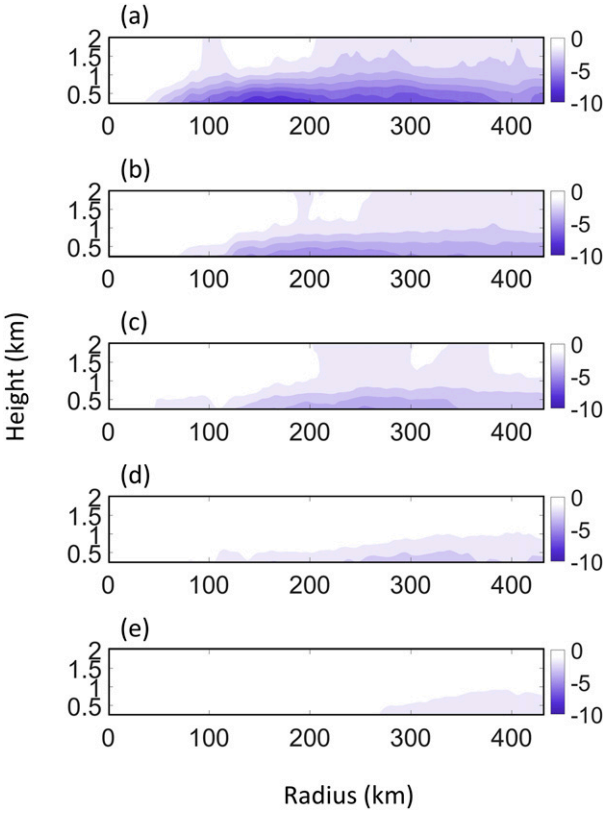

FIG. 15. The azimuthally averaged radial flow (shaded, m s^{-1}) at 35 h in (a) CTL, (b) ALLF70, (c) ALLF60, (d) ALLF50, and (e) ALLF40.

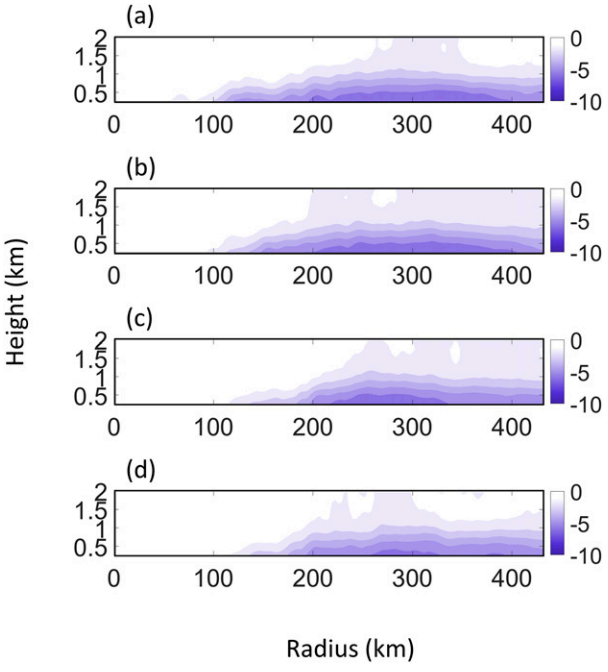

FIG. 16. As in Fig. 15, but for (a) R03F70, (b) R03F60, (c) R03F50, and (d) R03F40.

d. AAM transport

The AAM is connected to the TC wind field (Chan and Chan 2013; Tsuji et al. 2016). If more AAM can be transported into the TC from the environment, it is favorable for size increase. In our study, the evolution of AAM in each simulation is different. The AAM budget is shown below (Tuleya and Kurihara 1975):

$$\frac{\partial \overline{M}}{\partial t} = -\overline{r}\,\overline{M}\,\overline{\zeta}_a - \overline{w}\frac{\partial \overline{M}}{\partial z} - \overline{ru'\zeta'_a} - \overline{\frac{1}{\rho'}\frac{\partial P'}{\partial z}} + r\overline{F_\lambda}, \qquad (4)$$

where M is the absolute angular momentum, r is the radius, ζ_a is the absolute vorticity, w is the vertical velocity, ρ is the air density, p is the pressure, and F_λ is the tangential component of friction/diffusion. The most dominant component is the first term on the right-hand side which is the radial advection of AAM. The radial AAM transport is shown in Figs. 19–21. In ALL (Fig. 19), the thickness of the AAM import layer spans the range from 1.5 km in CTL to less than 1 km in ALLF40. More surface heat fluxes tend to result in a thicker AAM import layer (Figs. 19a–c). In ALLF40 and ALLF50, less surface heat fluxes are transported inward from the environment (Figs. 19d,e). Since the low-level inflow in CTL, ALLF70 and ALLF60 are stronger than those in ALLF40 and ALLF50, more AAM is transported by the inflow in CTL, ALLF70, and ALLF60. In R03 (Fig. 20), similar to ALL, the TCs with stronger low-level inflow have more AAM import. However, AAM is barely transported into the inner-core region within 150 km from the TC center in R03F40. The thickness of the AAM import layer differs among the simulations in R03. The AAM is deeper in R03F70 and shallower in R03F40 (1.5 and 1 km, respectively). In contrast to R03, AAM import in R36 is located in the inner-core region, whereas that in the outer-core region is much more limited. The AAM import in R36F70 in the inner-core region is 3 times of that in the outer-core region. In fact, the AAM import in the outer-core region in R36 varies with different surface heat fluxes. Specifically, there is a monotonic relationship between outer-core surface heat fluxes and AAM import. Although the surface heat fluxes in R03 are suppressed, AAM can still be transported inward from the environment, leading to an increase in size. However, since the AAM import is cut off in the R36 experiment, it is not favorable for TC wind field expansion.

Overall, the most critical location in which TC size is most influenced by surface heat fluxes is the outer-core region. In ALL, ALLF40 has less surface heat fluxes than CTL in the outer-core region, leading to less AAM import and also a smaller TC size. In R03, although the amount of surface heat fluxes is different among the simulations, the AAM import in the outer-core region is similar, leading to only slight differences in TC size. In R36, the surface heat fluxes in the outer-core region are different between the simulations. The TC size is smallest in R36F40 due to less inward transport of AAM, and largest in R36F70. This shows that surface heat fluxes in the outer-core region have the greatest impact on TC size.

Unauthenticated | Downloaded 06/06/22 05:55 PM UTC

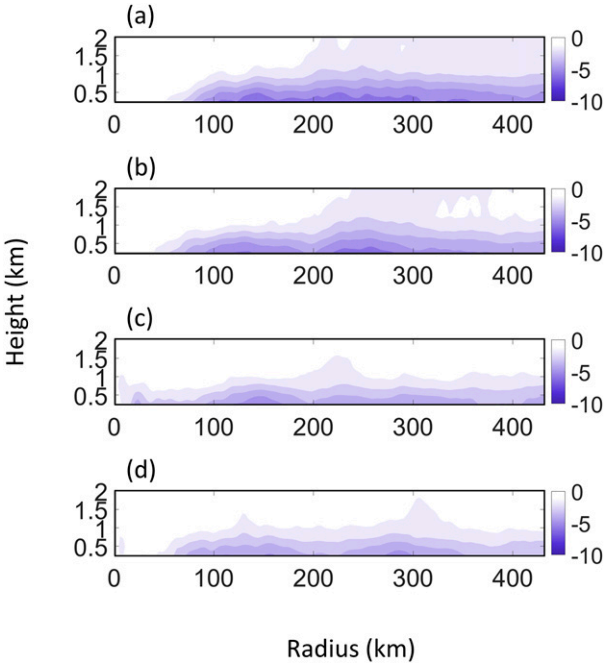

FIG. 17. As in Fig. 15, but for (a) R36F70, (b) R36F60, (c) R36F50, and (d) R36F40.

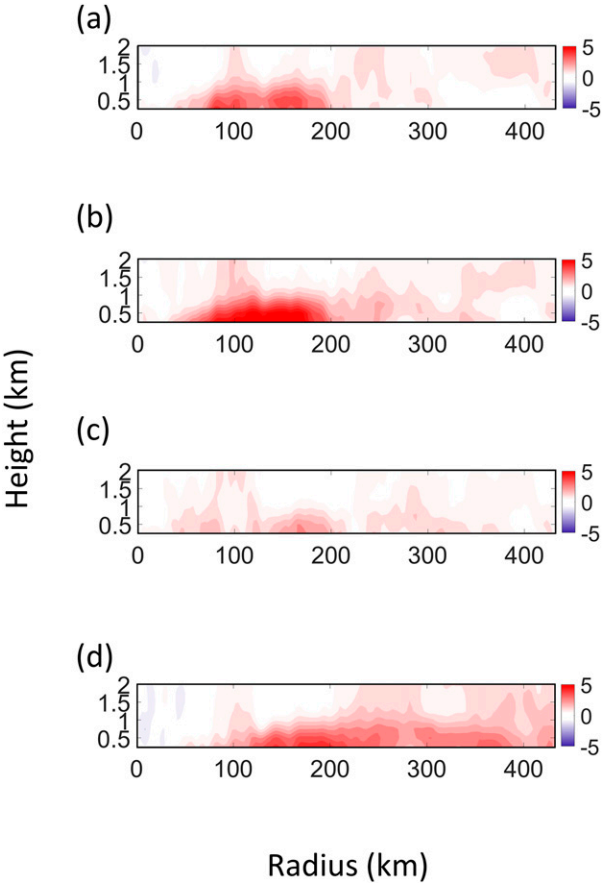

FIG. 18. The difference of azimuthally averaged radial flow (shaded, m s^{-1}) between CTL and each of (a) R03F70, (b) R03F40, (c) R36F70, and (d) R36F40.

Figure 21 summarizes the relation between surface heat fluxes and the TC wind field (e.g., intensity and size). If surface heat fluxes are suppressed in the inner-core region, the development of the inner rainbands would be inhibited, and therefore the latent heat release is reduced in that region. With a reduction in latent heat release, the secondary circulation becomes weaker, leading to weaker low-level inflow. In turn, the AAM import weakens, and with the weaker wind in the inner-core region, the enthalpy flux further weakens. This positive feedback loop can further impact the TC intensity (i.e., the WISHE mechanism). On the hand, the reduction of outer-core surface heat fluxes undergoes similar response to that in the inner core (i.e., the reduction of surface heat fluxes leads to the decrease of tangential wind where the surface heat fluxes are suppressed). In short, the surface heat fluxes in the outer core can influence TC size, following the same feedback mechanism on how the surface heat fluxes in the inner core affect TC intensity.

4. Conclusions

A case study of Typhoon Megi (2016) is conducted to investigate the relationship between surface heat fluxes (to mimic the WISHE mechanism) and TC size, and to understand the location in which TC size is most affected by the surface heat fluxes. A control run (CTL) and three groups of sensitivity experiments are conducted. The first group consists of experiments in which the surface heat fluxes are reduced in the entire innermost domain, collectively referred to as ALL. The second group, R03, includes experiments in which the surface heat fluxes are reduced in the inner-core region in the innermost domain. The surface heat fluxes in the last group, named R36, are suppressed in the outer-core region. Our results clearly indicate that only the surface heat fluxes in the outer-core region have a dominant impact on TC size.

In ALL, the development of inner and outer rainbands is inhibited when the surface heat fluxes are reduced in the entire innermost domain. This leads to a reduction in diabatic heat release in the rainbands. Because of the weaker radial gradient of diabetic heating, the secondary circulation including the low-level inflow weakens. Since the low-level inflow is too weak to transport a substantial amount of AAM into the TC, the TCs cease to grow. In R03, the surface heat fluxes are reduced only in the inner-core region, and thus only the rainbands in the inner-core region weaken. Consequently, the change of diabatic heating and the weakening of the secondary circulation are limited to the inner core. On the contrary, the low-level inflow does not change a lot in the outer-core region where the secondary circulation remains more or less the same. Therefore, the inflow is capable of transporting AAM inward, and the TC size increases. In R36, the results are similar to ALL since the outer rainbands are also suppressed due to the reduction of surface heat fluxes in the outer-core region. The outer rainbands, diabatic heating, secondary circulation and low-level inflow are weaker in the outer-core region in R36

Unauthenticated | Downloaded 06/06/22 05:55 PM UTC

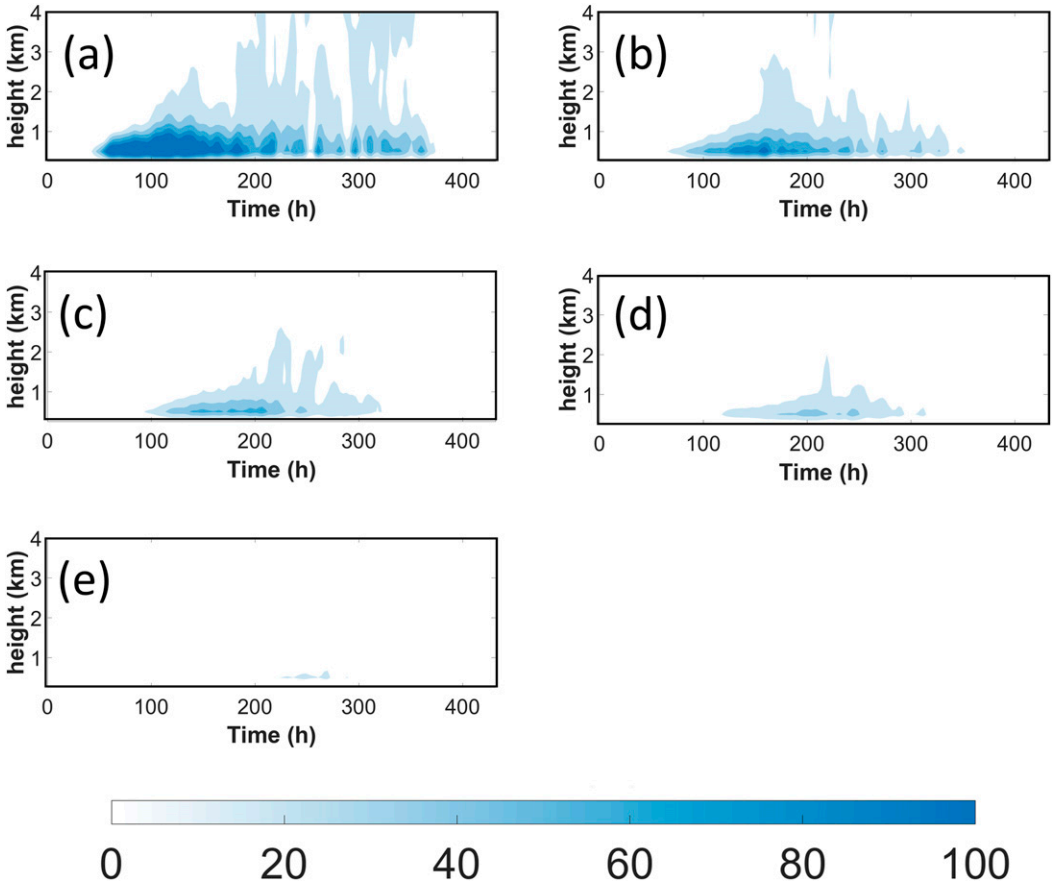

FIG. 19. The azimuthally averaged radial AAM transport (shaded, $m^2 s^{-2}$) at 35 h in (a) CTL, (b) ALLF70, (c) ALLF60, (d) ALLF50, and (e) ALLF40.

Unauthenticated | Downloaded 06/06/22 05:55 PM UTC

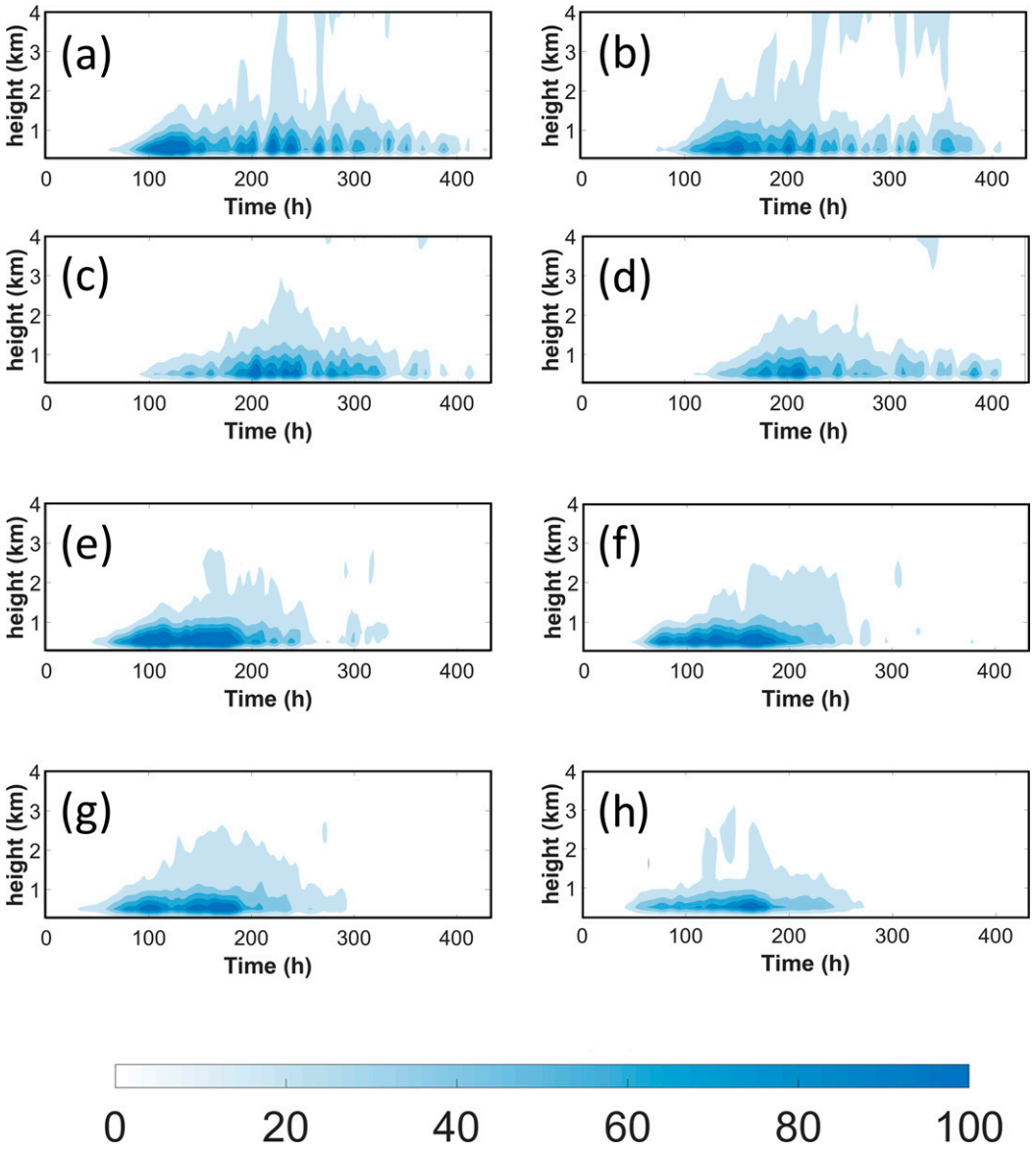

FIG. 20. As in Fig. 19, but for (a) R03F70, (b) R03F60, (c) R03F50, (d) R03F40, (e) R36F70, (f) R36F60, (g) R36F50, and (h) R36F40.

Unauthenticated | Downloaded 06/06/22 05:55 PM UTC

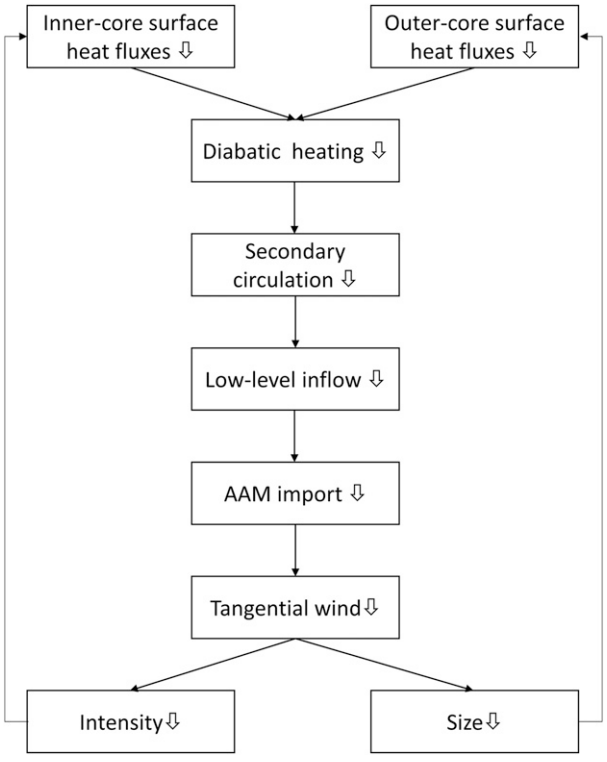

FIG. 21. The flowchart of the feedback between surface enthalpy flux and TC intensity/size.

experiments, which leads to insufficient AAM import and limited TC growth. With the reduced AAM import in the outer-core region, the wind speed decreases, thus weakening the TC's ability to extract surface heat fluxes from the ocean surface. This mechanism highlights the feedback loop between enthalpy flux and TC size in the outer-core region.

In all, the concept of WISHE applies not only to TC development in the inner-core region but also to TC size expansion in the outer-core region. Our study indicates that surface heat fluxes are crucial to the evolution of TC size. It also shows that the radial location of increased/decreased fluxes is what matters the most. Through our experiments, it can be inferred that the size change of TCs passing over a warm/cold ocean (eddy) needs to be investigated.

Acknowledgments. This work is supported by the Ministry of Science and Technology of Taiwan under Grants MOST 107-2111-M-002-016-MY3 and MOST 109-2123-M-002-003, and by the Office of Naval Research through Grant N00014-20-1-2467.

REFERENCES

Beljaars, A. C. M., 1995: The parameterization of surface fluxes in large-scale models under free convection. *Quart. J. Roy. Meteor. Soc.*, **121**, 255–270, https://doi.org/10.1002/qj.49712152203.

Chan, K. T., and J. C. Chan, 2012: Size and strength of tropical cyclones as inferred from QuikSCAT data. *Mon. Wea. Rev.*, **140**, 811–824, https://doi.org/10.1175/MWR-D-10-05062.1.

——, and ——, 2013: Angular momentum transports and synoptic flow patterns associated with tropical cyclone size change. *Mon. Wea. Rev.*, **141**, 3985–4007, https://doi.org/10.1175/MWR-D-12-00204.1.

——, and ——, 2014: Impacts of initial vortex size and planetary vorticity on tropical cyclone size. *Quart. J. Roy. Meteor. Soc.*, **140**, 2235–2248, https://doi.org/10.1002/qj.2292.

——, and ——, 2015: Global climatology of tropical cyclone size as inferred from QuikSCAT data. *Int. J. Climatol.*, **35**, 4843–4848, https://doi.org/10.1002/joc.4307.

Chavas, D. R., and K. A. Emanuel, 2010: A QuikSCAT climatology of tropical cyclone size. *Geophys. Res. Lett.*, **37**, L18816, https://doi.org/10.1029/2010GL044558.

Chen, J., and D. R. Chavas, 2020: The transient responses of an axisymmetric tropical cyclone to instantaneous surface roughening and drying. *J. Atmos. Sci.*, **77**, 2807–2834, https://doi.org/10.1175/JAS-D-19-0320.1.

Cheng, C.-J., and C.-C. Wu, 2018: The role of WISHE in secondary eyewall formation. *J. Atmos. Sci.*, **75**, 3823–3841, https://doi.org/10.1175/JAS-D-17-0236.1.

——, and ——, 2020: The role of WISHE in the rapid intensification of tropical cyclones. *J. Atmos. Sci.*, **77**, 3139–3160, https://doi.org/10.1175/JAS-D-20-0006.1.

Cronin, T. W., and D. R. Chavas, 2019: Dry and semidry tropical cyclones. *J. Atmos. Sci.*, **76**, 2193–2212, https://doi.org/10.1175/JAS-D-18-0357.1.

D'Asaro, E. A., and Coauthors, 2013: Impact of typhoons on the ocean in the Pacific: ITOP. *Bull. Amer. Meteor. Soc.*, **95**, 1405–1418, https://doi.org/10.1175/BAMS-D-12-00104.1.

Dyer, A. J., and B. B. Hicks, 1970: Flux–gradient relationships in the constant flux layer. *Quart. J. Roy. Meteor. Soc.*, **96**, 715–721, https://doi.org/10.1002/qj.49709641012.

Emanuel, K. A., 1986: An air–sea interaction theory for tropical cyclones. Part I: Steady-state maintenance. *J. Atmos. Sci.*, **43**, 585–605, https://doi.org/10.1175/1520-0469(1986)043<0585:AASITF>2.0.CO;2.

——, 1989: The finite-amplitude nature of tropical cyclogenesis. *J. Atmos. Sci.*, **46**, 3431–3456, https://doi.org/10.1175/1520-0469(1989)046<3431:TFANOT>2.0.CO;2.

——, M. Fantini, and A. J. Thorpe, 1987: Baroclinic instability in an environment of small stability to slantwise moist convection. Part I: Two-dimensional models. *J. Atmos. Sci.*, **44**, 1559–1573, https://doi.org/10.1175/1520-0469(1987)044<1559:BIIAEO>2.0.CO;2.

Frisius, T., 2015: What controls the size of a tropical cyclone? Investigations with an axisymmetric model. *Quart. J. Roy. Meteor. Soc.*, **141**, 2457–2470, https://doi.org/10.1002/qj.2537.

Hill, K. A., and G. M. Lackmann, 2009: Influence of environmental humidity on tropical cyclone size. *Mon. Wea. Rev.*, **137**, 3294–3315, https://doi.org/10.1175/2009MWR2679.1.

Holland, G. J., and R. T. Merrill, 1984: On the dynamics of tropical cyclone structural changes. *Quart. J. Roy. Meteor. Soc.*, **110**, 723–745, https://doi.org/10.1002/qj.49711046510.

Hong, S., Y. Noh, and J. Dudhia, 2006: A new vertical diffusion package with an explicit treatment of entrainment processes. *Mon. Wea. Rev.*, **134**, 2318–2341, https://doi.org/10.1175/MWR3199.1.

Iacono, M. J., E. J. Mlawer, S. A. Clough, and J.-J. Morcrette, 2000: Impact of an improved longwave radiation model, RRTM, on the energy budget and thermodynamic properties of the NCAR Community Climate Model, CCM3. *J. Geophys. Res.*, **105**, 14 873–14 890, https://doi.org/10.1029/2000JD900091.

Ito, K., Y. Ishikawa, Y. Miyamoto, and T. Awaji, 2011: Short-time-scale processes in a mature hurricane as a response to sea surface fluctuations. *J. Atmos. Sci.*, **68**, 2250–2272, https://doi.org/10.1175/JAS-D-10-05022.1.

Unauthenticated | Downloaded 06/06/22 05:55 PM UTC

Jiménez, P., J. Dudhia, J. F. Gonzàlez-Rouco, and J. Navarro, 2012: A revised scheme for the WRF surface layer formulation. *Mon. Wea. Rev.*, **140**, 898–918, https://doi.org/10.1175/MWR-D-11-00056.1.

Kain, J. S., 2004: The Kain–Fritsch convective parameterization: An update. *J. Appl. Meteor.*, **43**, 170–181, https://doi.org/10.1175/1520-0450(2004)043<0170:TKCPAU>2.0.CO;2.

——, and J. M. Fritsch, 1990: A one-dimensional entraining/detraining plume model and its application in convective parameterization. *J. Atmos. Sci.*, **47**, 2784–2802, https://doi.org/10.1175/1520-0469(1990)047<2784:AODEPM>2.0.CO;2.

Knaff, J. A., S. P. Longmore, and D. A. Molenar, 2014: An objective satellite-based tropical cyclone size climatology. *J. Climate*, **27**, 455–476, https://doi.org/10.1175/JCLI-D-13-00096.1.

Lee, C., K. K. Cheung, W. Fang, and R. L. Elsberry, 2010: Initial maintenance of tropical cyclone size in the western North Pacific. *Mon. Wea. Rev.*, **138**, 3207–3223, https://doi.org/10.1175/2010MWR3023.1.

Lin, I.-I., C.-H. Chen, I.-F. Pun, W. T. Liu, and C.-C. Wu, 2009: Warm ocean anomaly, air sea fluxes, and the rapid intensification of Tropical Cyclone Nargis. *Geophys. Res. Lett.*, **36**, L03817, https://doi.org/10.1029/2008GL035815.

——, M.-D. Chou, and C.-C. Wu, 2011: The impact of a warm ocean eddy on Typhoon Morakot (2009)—A preliminary study from satellite observations and numerical modeling. *Terr. Atmos. Oceanic Sci.*, **22**, 661–671, https://doi.org/10.3319/TAO.2011.08.19.01(TM).

——, and Coauthors, 2013: An ocean coupling potential intensity index for tropical cyclones. *Geophys. Res. Lett.*, **40**, 1878–1882, https://doi.org/10.1002/grl.50091.

Liu, K. S., and J. C. Chan, 2002: Synoptic flow patterns associated with small and large tropical cyclones over the western North Pacific. *Mon. Wea. Rev.*, **130**, 2134–2142, https://doi.org/10.1175/1520-0493(2002)130<2134:SFPAWS>2.0.CO;2.

Lu, X., H. Yu, and X. Lei, 2011: Statistics for size and radial wind profile of tropical cyclones in the western North Pacific. *Acta Meteor. Sin.*, **25**, 104–112, https://doi.org/10.1007/s13351-011-0008-9.

Ma, Z., J. Fei, L. Liu, X. Huang, and X. Cheng, 2013: Effects of the cold core eddy on tropical cyclone intensity and structure under idealized air–sea interaction conditions. *Mon. Wea. Rev.*, **141**, 1285–1303, https://doi.org/10.1175/MWR-D-12-00123.1.

——, ——, X. Huang, and X. Cheng, 2015: Contributions of surface sensible heat fluxes to tropical cyclone. Part I: Evolution of tropical cyclone intensity and structure. *J. Atmos. Sci.*, **72**, 120–140, https://doi.org/10.1175/JAS-D-14-0199.1.

Marks, F., and Coauthors, 1998: Landfalling tropical cyclones: Forecast problems and associated research opportunities. *Bull. Amer. Meteor. Soc.*, **79**, 305–323, https://doi.org/10.1175/1520-0477(1998)079<0305:LTCFPA>2.0.CO;2.

Neelin, J. D., I. M. Held, and K. H. Cook, 1987: Evaporation–wind feedback and low-frequency variability in the tropical atmosphere. *J. Atmos. Sci.*, **44**, 2341–2348, https://doi.org/10.1175/1520-0469(1987)044<2341:EWFALF>2.0.CO;2.

Paulson, C. A., 1970: The mathematical representation of wind speed and temperature profiles in the unstable atmospheric surface layer. *J. Appl. Meteor.*, **9**, 857–861, https://doi.org/10.1175/1520-0450(1970)009<0857:TMROWS>2.0.CO;2.

Peng, C.-H., and C.-C. Wu, 2020: The impact of outer-core surface heat fluxes on the convective activities and rapid intensification of tropical cyclones. *J. Atmos. Sci.*, **77**, 3907–3927, https://doi.org/10.1175/JAS-D-19-0348.1.

Powell, M. D., P. J. Vickery, and T. A. Reinhold, 2003: Reduced drag coefficient for high wind speeds in tropical cyclones. *Nature*, **422**, 279–283, https://doi.org/10.1038/nature01481.

Radu, R., R. Toumi, and J. Phau, 2014: Influence of atmospheric and sea-surface temperature on the size of Hurricane Catarina. *Quart. J. Roy. Meteor. Soc.*, **140**, 1778–1784, https://doi.org/10.1002/qj.2232.

Riehl, H., 1950: A model for hurricane formation. *J. Appl. Phys.*, **21**, 917–925, https://doi.org/10.1063/1.1699784.

Ruiz-Arias, J., J. Dudhia, F. J. Santos-Alamillos, and D. Pozo-Vázquez, 2013: Surface clear-sky shortwave radiative closure intercomparisons in the Weather Research and Forecasting Model. *J. Geophys. Res. Atmos.*, **118**, 9901–9913, https://doi.org/10.1002/jgrd.50778.

Schenkel, B. A., 2017: Are multiple tropical cyclone events similar among basins? *J. Climate*, **30**, 5805–5813, https://doi.org/10.1175/JCLI-D-17-0088.1.

Shen, L.-Z., and C.-C. Wu, 2018: The effect of surface heat fluxes in the outer region on the size of Typhoon Megi (2016). *33rd Conf. on Hurricanes and Tropical Meteorology*, Ponte Vedra, FL, Amer. Meteor. Soc., 5C.7, https://ams.confex.com/ams/33HURRICANE/webprogram/Paper339441.html.

Tsuji, H., H. Itoh, and K. Nakajima, 2016: Mechanism governing the size change of tropical cyclone-like vortices. *J. Meteor. Soc. Japan*, **94**, 219–236, https://doi.org/10.2151/jmsj.2016-012.

Tuleya, R. E., and Y. Kurihara, 1975: The energy and angular momentum budgets of a three-dimensional tropical cyclone model. *J. Atmos. Sci.*, **32**, 287–301, https://doi.org/10.1175/1520-0469(1975)032<0287:TEAAMB>2.0.CO;2.

Wang, Y., and C.-C. Wu, 2004: Current understanding of tropical cyclone structure and intensity changes—A review. *Meteor. Atmos. Phys.*, **87**, 257–278, https://doi.org/10.1007/s00703-003-0055-6.

Webb, E. K., 1970: Profile relationships: The log-linear range, and extension to strong stability. *Quart. J. Roy. Meteor. Soc.*, **96**, 67–90, https://doi.org/10.1002/qj.49709640708.

Willoughby, H. E., 1995: Mature structure and evolution. Global perspectives on tropical cyclones, WMO Tech. Doc. WMO/TD-693, 21–62.

Wu, C.-C., C.-Y. Lee, and I.-I. Lin, 2007: The effect of the ocean eddy on tropical cyclone intensity. *J. Atmos. Sci.*, **64**, 3562–3578, https://doi.org/10.1175/JAS4051.1.

——, W.-T. Tu, I.-F. Pun, I.-I. Lin, and M. S. Peng, 2016: Tropical cyclone-ocean interaction in Typhoon Megi (2010)—A synergy study based on ITOP observations and atmosphere-ocean coupled model simulations. *J. Geophys. Res. Atmos.*, **121**, 153–167, https://doi.org/10.1002/2015JD024198.

Xu, J., and Y. Wang, 2010a: Sensitivity of tropical cyclone inner-core size and intensity to the radial distribution of surface entropy flux. *J. Atmos. Sci.*, **67**, 1831–1852, https://doi.org/10.1175/2010JAS3387.1.

——, and ——, 2010b: Sensitivity of the simulated tropical cyclone inner-core size to the initial vortex size. *Mon. Wea. Rev.*, **138**, 4135–4157, https://doi.org/10.1175/2010MWR3335.1.

Zhang, D.-L., and R. A. Anthes, 1982: A high–resolution model of the planetary boundary layer—Sensitivity tests and comparisons with SESAME-79 data. *J. Appl. Meteor.*, **21**, 1594–1609, https://doi.org/10.1175/1520-0450(1982)021<1594:AHRMOT>2.0.CO;2.

Zhang, F., and K. Emanuel, 2016: On the role of surface fluxes and WISHE in tropical cyclone intensification. *J. Atmos. Sci.*, **73**, 2011–2019, https://doi.org/10.1175/JAS-D-16-0011.1.

Unauthenticated | Downloaded 06/06/22 05:55 PM UTC